

# Impact of Nonfullerene Acceptor Core Structure on the Photophysics and Efficiency of Polymer Solar Cells

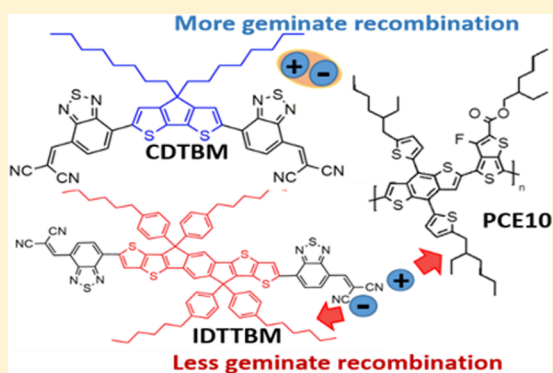
Maha A. Alamoudi,<sup>†</sup> Jafar I. Khan,<sup>†</sup> Yuliar Firdaus,<sup>†</sup> Kai Wang,<sup>†</sup> Denis Andrienko,<sup>‡</sup> Pierre M. Beaujuge,<sup>†</sup> and Frédéric Laquai\*<sup>†</sup>

<sup>†</sup>King Abdullah University of Science and Technology (KAUST), KAUST Solar Center (KSC), Physical Sciences and Engineering Division (PSE), Material Science and Engineering Program (MSE), Thuwal 23955-6900, Kingdom of Saudi Arabia

<sup>‡</sup>Max Planck Institute for Polymer Research (MPIP), Ackermannweg 10, D-55128 Mainz, Germany

## S Supporting Information

**ABSTRACT:** Small-molecule “nonfullerene” acceptors are promising alternatives to fullerene (PC61/71BM) derivatives often used in bulk heterojunction (BHJ) organic solar cells; yet, the efficiency-limiting processes and their dependence on the acceptor structure are not clearly understood. Here, we investigate the impact of the acceptor core structure (cyclopenta-[2,1-b:3,4-b']dithiophene (CDT) versus indacenodithiophene (IDTT)) of malononitrile (BM)-terminated acceptors, namely CDTBM and IDTTBM, on the photophysical characteristics of BHJ solar cells. Using PCE10 as donor polymer, the IDTT-based acceptor achieves power conversion efficiencies (8.4%) that are higher than those of the CDT-based acceptor (5.6%) because of a concurrent increase in short-circuit current and open-circuit voltage. Using (ultra)fast transient spectroscopy we demonstrate that reduced geminate recombination in PCE10:IDTTBM blends is the reason for the difference in short-circuit currents. External quantum efficiency measurements indicate that the higher energy of interfacial charge-transfer states observed for the IDTT-based acceptor blends is the origin of the higher open-circuit voltage.



Organic photovoltaic (OPV) devices are predominantly based on solution-processed bulk heterojunction (BHJ) photoactive layers, typically composed of an electron-donor, a conjugated polymer or small molecule, and an electron-acceptor molecule, often a fullerene PC<sub>61/71</sub>BM.<sup>1–3</sup> Until recently, fullerene derivatives prevailed as acceptors for high-performance OPV devices,<sup>4–9</sup> while device efficiencies with “nonfullerene acceptors” (NFAs) remained limited.<sup>10,11</sup> However, NFAs have now reached performance parity with fullerene acceptors, and several materials even outperform fullerenes in terms of efficiency and (photo)stability.<sup>12–19</sup> Very recently, a new record efficiency of 13% achieved with novel NFAs has been demonstrated.<sup>20</sup> Owing to the demonstration of higher power conversion efficiencies achieved with NFAs, efforts to design and synthesize novel NFAs have considerably increased.<sup>21–23</sup>

Several advantages such as lower costs, the possibility of tuning the band gap,<sup>24</sup> strong optical absorption,<sup>25</sup> and improved photostability are key factors making NFAs very attractive.<sup>26</sup> In fact, when the optical and electronic properties are tuned, open-circuit voltages,  $V_{OC}$ ,<sup>27</sup> often higher than those

achieved with fullerene acceptors can be obtained. Furthermore, the increased absorption of the photoactive layer and the broader spectral coverage of the solar spectrum should be conducive to short-circuit current densities,  $J_{SC}$ ,<sup>28</sup> that are higher than those possible with fullerenes. Better control over the acceptor’s energy levels with respect to the donor material can help to further increase the power conversion efficiencies,<sup>29</sup> which is not trivial when fullerene-based acceptors are used.

Among the vast number of donor polymers available to date, PCE10 is now widely used as a model system in OPV devices.<sup>30</sup> Applications of PCE10 as donor polymer in solar cells with fullerene acceptors have yielded power conversion efficiencies of up to 10%. Nevertheless, implementation of NFAs in conjunction with PCE10 is still limited, and even more limited is the insight into the photophysical processes that determine the efficiency of PCE10:NFA devices. In short, our general understanding of the physical processes occurring in BHJ solar

Received: January 11, 2018

Accepted: March 2, 2018

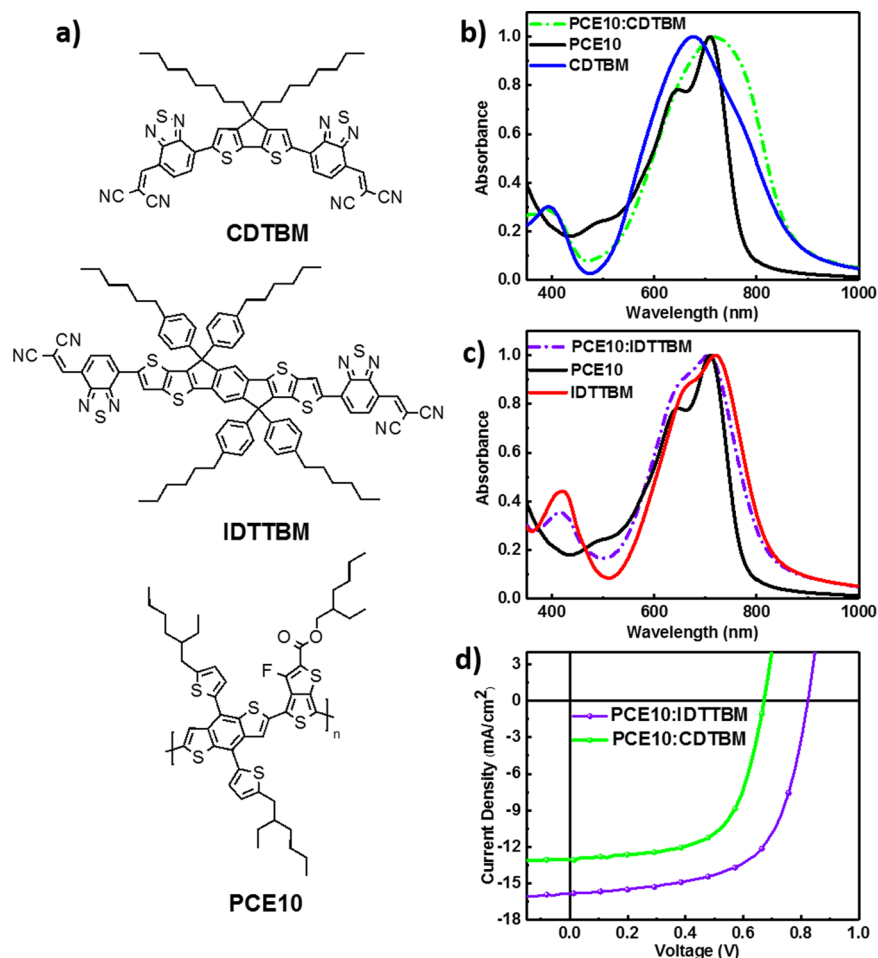


**Figure 1.** (a) Chemical structures of the nonfullerene acceptor molecules CDTBM, and IDTTBM and of the donor polymer PCE10. (b) Normalized steady-state UV-vis absorption spectra of neat PCE10, CDTBM, and PCE10:CDTBM (2:3 w/w) blends. (c) Normalized UV-vis absorption of neat PCE10, IDTTBM, and PCE10:IDTTBM (1:1 w/w) blends. (d) *J*-*V* characteristics of PCE10:CDTBM and PCE10:IDTTBM devices.

cells is as follows: photoexcitation of the bulk heterojunction creates bound electron-hole pairs (Frenkel-type excitons).<sup>31,32</sup> The excitons dissociate at the donor-acceptor interface, which in intimately mixed blends leads to ultrafast exciton quenching on a time scale of less than 100 femtoseconds (fs). Exciton quenching by interfacial charge transfer eventually leads to the formation of interfacial charge-transfer (CT) states and spatially separated (free) charge carriers.<sup>33</sup> Ultimately, the free charges drift-diffuse through the donor and acceptor network and are collected at the electrodes, resulting in a photocurrent in the external circuit. However, in the case of large-scale donor-acceptor demixing, diffusion of excitons can also be observed on the time scale of several picoseconds (ps) in addition to ultrafast dissociation.<sup>34</sup> Furthermore, CT states generated upon charge transfer at the interface may not dissociate entirely into free charges, if the charges cannot overcome their mutual Coulomb attraction. These CT states recombine geminately, typically on the time scale of hundreds of picoseconds to several nanoseconds. Recent theoretical insights into what determines the efficiency of the interfacial CTstate dissociation have demonstrated that the driving force for the CTstate splitting depends on the quadrupole moments of the donor and acceptor, as well as roughness of the interface.<sup>35-38</sup> Furthermore, free charge carrier extraction competes with nongeminate recombination, potentially leading to low fill

factors.<sup>34</sup> Both geminate and nongeminate recombinations are loss channels that reduce the quantum efficiency of the solar cell. From a spectroscopic viewpoint, geminate and nongeminate recombinations can be distinguished by the different response of their dynamics to the light intensity. CT states are Coulombically bound charges localized and immobilized at the donor-acceptor interface. Hence, their decay is typically fluence-independent. In contrast, nongeminate recombination of free charge carriers is more probable at higher carrier densities, i.e., at higher light intensities. Nongeminate recombination can also lead to the population of the triplet state, as spin correlation is lost when charges are fully separated, and recombination of free charges follows spin-statistics leading to preferential triplet state formation, which can impact device performance and stability.

In this study, we investigate the impact of the chemical structure of the NFA core on the photophysical processes that determine the device efficiency. Blending the small-molecule (SM) acceptor IDTTBM and the commercial low band gap polymer donor PCE10 yields power conversion efficiencies in excess of 8%, efficiencies that are significantly higher than those achieved with the structurally related SM acceptor CDTBM that has been reported previously by us.<sup>39</sup> Here, we use PCE10 as donor polymer for reasons of consistency with our previous study on CDTBM, which showed good device performance.

**Table 1. Figures of Merit of Optimized PCE10:CDTBM (2:3 w/w) and PCE10:IDTTBM (1:1 w/w) Devices**

photovoltaic blend	D/A ratio	$V_{oc}$ [V]	$J_{sc}$ [mA/cm <sup>2</sup> ]	$J_{sc}(EQE)^a$ [mA/cm <sup>2</sup> ]	FF [%]	max. PCE [%]
PCE10:CDTBM	2:3	0.67 ± 0.01	12.7 ± 0.4	12.5 ± 0.4	62 ± 1.3	5.6
PCE10:IDTTBM	1:1	0.83 ± 0.01	15.5 ± 0.34	15.8 ± 0.4	63 ± 1.3	8.4

<sup>a</sup>The  $J_{sc}$  Calculated from EQE

Furthermore, we focus on the comparison of the impact of the acceptor's core structure on the device performance and photophysics rather than on further optimization of the performance when combined with different donor polymers. Specifically, we employ optical spectroscopy, including time-resolved photoluminescence and transient absorption (TA) spectroscopy, to disentangle the various charge generation and recombination channels and to examine their impact on device performance in these two structurally related systems. Our findings indicate that 90% of the charges generated upon photoexcitation in the PCE10:IDTTBM blend system are spatially separated and undergo nongeminate recombination, if not extracted, compared to 71% in the PCE10:CDTBM blend system. This is in excellent agreement with the internal quantum efficiencies (IQE) determined for the two blend systems in actual BHJ solar cells, precisely 90% versus 74%, implying that geminate recombination is a more significant loss channel in PCE10:CDTBM, leading to lower photocurrents. Our experimental results are supported by theoretical calculations, which demonstrate a larger quadrupole moment of the IDTTBM acceptor, which in turn improves CTstate dissociation, as well as smaller energetic disorder in IDTTBM domains, favoring more efficient electron transport and smaller  $V_{oc}$  reduction. In fact, the energy of the interfacial CT states is found to be higher in PCE10:IDTTBM, largely explaining the difference in the open-circuit voltage between the two systems. Finally, we conclude that field-dependent generation or nongeminate recombination competing with extraction are not major loss channels in these blends, which is consistent with their fill factors in excess of 60%.

**Materials and Device Performance.** The steady-state absorption spectra of PCE10 and the NFAs in neat films and the  $J$ - $V$  characteristics of optimized PCE10:NFA devices are provided in Figure 1. The CDTBM and IDTTBM acceptors carry the same terminal (2-(benzo[*c*][1,2,5]-thiadiazol-4-ylmethylene)-malononitrile) electron-withdrawing groups (BM) (Figure 1a), appended because of their strong electron-withdrawing character, resulting in low-lying lowest unoccupied molecular orbital (LUMO) energy levels. The principal structural difference between the CDTBM<sup>39</sup> and IDTTBM<sup>40</sup> acceptors is their core: CDTBM uses cyclopenta-[2,1-*b*:3,4-*b'*]-dithiophene (CDT) as the core, and IDTTBM uses a more extended indacenodithiophene (IDTT) core.

Steady-state absorption spectra of neat PCE10 films, CDTBM films, and PCE10:CDTBM blends alongside the respective IDTTBM and PCE10:IDTTBM samples are shown in panels b and c of Figure 1, respectively. The absorption of PCE10 is broad, ranging from 550 to 780 nm, with vibronic peaks at 644 and 710 nm. CDTBM exhibits a broad absorption band peaking at 677 nm; however, a clear vibronic structure is not observed. IDTTBM films absorb mostly in the spectral region from 550 to 850 nm, with a peak absorption at 677 nm and a vibronic progression at 663 nm. Comparing the absorption spectrum of PCE10 with both acceptors shows that their absorption largely overlaps. However, CDTBM has a broader absorption than IDTTBM, extending further into the

spectral region of 800–900 nm, as shown in Figure 1b. Hence, the PCE10:CDTBM blend's absorption spectrum extends also further into the red spectral region, peaking at 722 nm, compared to that of the PCE10:IDTTBM blend, which peaks at 720 nm. The reason for the lower-energy absorption of CDTBM compared to the absorption of IDTTBM is not obvious. However, aggregation of the smaller acceptor core structure of CDTBM in the solid state could lead to a red-shift of the absorption spectrum, which also explains the rather featureless shape of the absorption spectrum.

Thin-film BHJ solar cells with inverted device structures, ITO/*a*-ZnO<sup>41</sup>/PCE10:SM/MoO<sub>3</sub>/Ag, and a device area of 0.1 cm<sup>2</sup> were fabricated and tested under AM1.5G solar illumination at an irradiance of 100 mW/cm<sup>2</sup>. More specifically, CDTBM-based cells were fabricated according to the optimized conditions reported in our previous work (2:3 w/w).<sup>39</sup> This material system was cast from chlorobenzene (CB) with 0.8% 1-chloronaphthalene (CN) as additive, whereas optimized PCE10:IDTTBM blend BHJ devices (1:1 w/w) were cast from CB (cf. details in the Supporting Information). Figure 1d depicts the current density–voltage ( $J$ - $V$ ) characteristics of optimized CDTBM and IDTTBM-based BHJ solar cells with PCE10 as the polymer donor. As previously reported, optimized PCE10:CDTBM devices reached maximum PCEs of up to 5%.<sup>39</sup> Here, the PCE has been improved further compared to our previous work, to average PCE values of 5.3% (max. PCE 5.6%), a short-circuit current ( $J_{sc}$ ) of 12.7 mA/cm<sup>2</sup>, an open-circuit voltage ( $V_{oc}$ ) of 0.67 V, and a fill factor (FF) of 62%, as shown in Table 1. BHJ devices made with the IDTTBM acceptor achieved higher average PCEs of 8.1% with a maximum value of 8.4% because of higher  $J_{sc}$  > 15 mA/cm<sup>2</sup>, increased  $V_{oc}$  of 0.83 V, and similar FF of 63%.

The  $J_{sc}$  values measured from optimized CDTBM and IDTTBM-based BHJ solar cells (Table 1) are consistent with the corresponding values from spectrally integrated external quantum efficiency (EQE) measurements presented in Figure S1. From ellipsometry measurements and transfer matrix simulations, the maximum  $J_{sc}$  was estimated as 18.5 mA/cm<sup>2</sup> for PCE10:CDTBM (2:3 w/w) and 18.6 mA/cm<sup>2</sup> for PCE10:IDTTBM (1:1 w/w) for their respective optimal thicknesses (≈65 nm and ≈80 nm, respectively). Further details of the ellipsometry experiments are presented in Figures S2 and S3. The strong photoresponse from both devices in the spectral region of 1.55–2.2 eV is consistent with the absorption spectra of the materials, as shown in Figure 1b,c. The corresponding internal quantum efficiency spectra inferred from EQE and blend absorbance as determined from a combination of data from photothermal deflection spectroscopy (PDS) and ultraviolet–visible (UV–vis) spectrophotometry experiments are shown in Figure 2a,b. Here, the IQE was calculated from the EQE signal and the absorbance  $A(E)$ ,<sup>42</sup> further details are given in the Supporting Information. Maximum IQE values of 74% for CDTBM and 90% for IDTTBM were found in the range of 1.6–2.2 eV. The low-energy tail of the sensitive EQE measurement was fitted with a Gaussian to determine the CTstate energy according to the

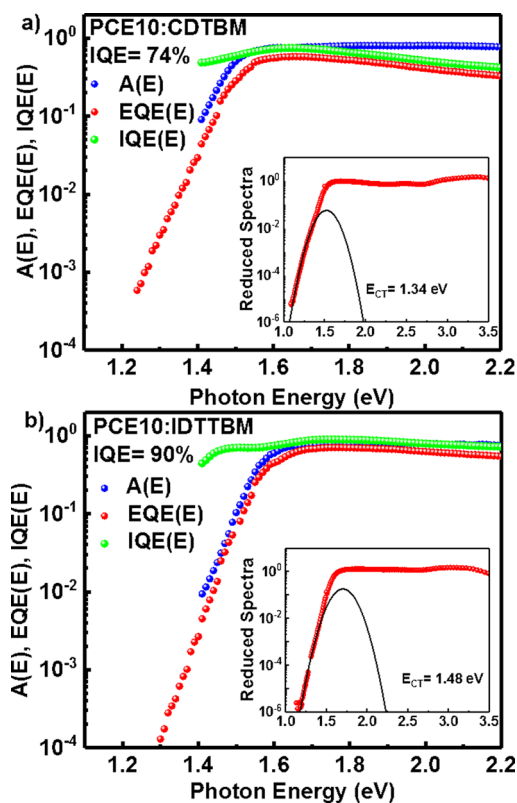


Figure 2. Steady-state blend absorbance  $A(E)$  determined by PDS and UV-vis measurements, sensitive  $EQE(E)$  measurements, and the calculated  $IQE(E)$  of (a) PCE10:CDTBM and (b) PCE10:IDTTBM devices. The insets display the sensitive  $EQE$  data fitted with a Gaussian to obtain the CT state energy.

method previously described by Vandewal et al.<sup>43</sup> The estimated values of the CT state energy are 1.34 and 1.48 eV for PCE10:CDTBM and PCE10:IDTTBM, respectively. We note that the difference in CT state energy can (to a large extent) be ascribed to the difference in LUMO energies between the two acceptors:  $-4.27$  eV for CDTBM and  $-4.03$  eV for IDTTBM as determined from cyclic voltammetry measurements and the absorption onset of the materials. As can be seen from Figure 2, the  $IQE$  response for PCE10:IDTTBM and PCE10:CDTBM steadily decreased below the band gap. As reference, we determined the  $IQE$  characteristics for the system PCE10:PCBM, shown in Figure S4. We confirmed that the  $IQE$  remains high even below the band gap of the blend, as reported earlier for many other polymer:fullerene blends.<sup>42</sup> The reason for the steady drop of the  $IQE$  observed for the PCE10:NFA blends requires further studies. Here we conclude from our measurements that the observed difference in CT state energies explains well the difference in open-circuit voltage observed for the two systems.

**Density Functional Theory Calculations.** We performed density functional theory (DFT) calculations using the B3LYP functional and 6-311g(d,p) basis set. Optimized geometries of CDTBM and IDTTBM in their neutral states are shown in Figure S5. For CDTBM we show three conformers with different orientations of the BM groups with respect to the core. The lowest-energy conformer (formation energies are summarized in Table S1) is CDTBM-tt. This conformer has a large dipole moment of approximately 10 D. The second lowest in energy conformer, CDTBM-ct, has practically no dipole moment, while the third conformer, CDTBM-cc, has a dipole moment of ca. 4 D. IDTTBM has no dipole moment in its lowest-energy conformation. The reason for the absence or presence of the dipole moment in the ground state is the symmetry of the conjugated core of the donor. The CDT

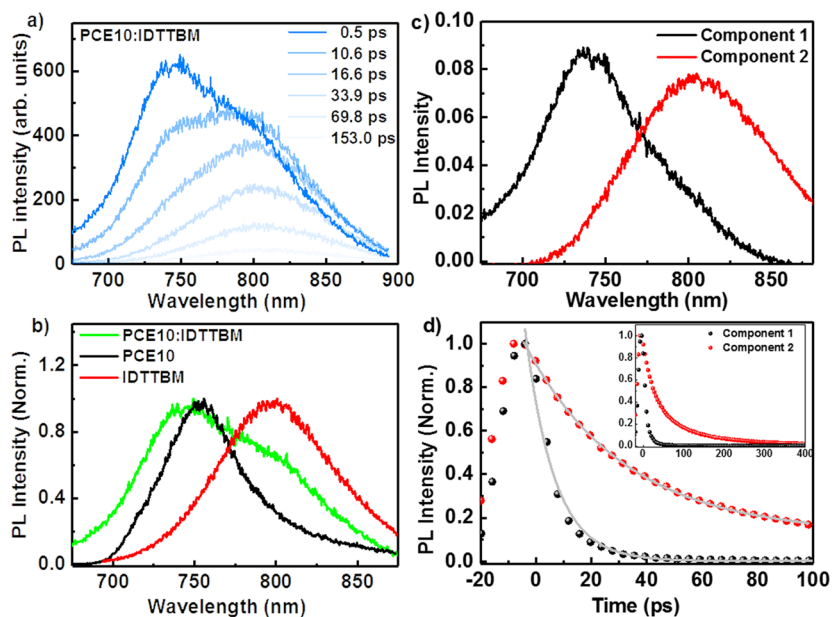


Figure 3. Time-resolved photoluminescence data of the PCE10:IDTTBM system: (a) Picosecond time-resolved spectra after excitation at 600 nm (delay times denoted in the legend). (b) Time-integrated spectra of a neat PCE10 film, IDTTBM film, and PCE10:IDTTBM blend. (c) Component spectra obtained by multivariate curve resolution (MCR) analysis of PCE10:IDTTBM blend PL spectra. Component 1 is assigned to photoluminescence from PCE10, and component 2 is assigned to PL from IDTTBM because of the spectral similarity to the emission of neat film shown in panel b. (d) Transients of components fitted with single-exponential decays. The inset describes a larger time window up to 400 ps.

has a mirror symmetry (reflection in the  $zy$ -plane), while the conjugated core of the IDTT donor has an inversion center. Because S and N heteroatoms coordinate better with hydrogens, the ground states of the entire molecules have a mirror or an inversion symmetry, including the BM groups. This symmetry determines whether the dipole moments of two donor–acceptor subunits compensate each other or not. The ground-state dipole moment has a clear impact on the width of the density of states: larger dipole moments lead to broader density of states, which typically has an effect on the charge carrier mobility. In addition, a broader density of states leads to a reduction of the chemical potential of holes in the acceptor and thus a larger reduction of  $V_{OC}$  with respect to the photovoltaic gap, namely  $IP_{donor} - EA_{acceptor}$ , which is also observed experimentally (see above). CDTBM and IDTTBM have different lengths of conjugated donor cores. A direct implication of this is a much larger value of the quadrupole tensor. The actual values of the diagonal elements of the quadrupole tensor are also given in Table S1. The quadrupole moment affects both the solid-state energy level alignment and the efficiency of the CTstate splitting.<sup>35–38</sup> The exact effect on the CT state splitting and level alignment depends on the orientation of acceptor molecules at the interface. If we assume, for both CDTBM and IDTTBM, a particular orientation that helps splitting CT states (as both solar cells are efficient), the quadrupole moment of IDTTBM is almost twice as large as that of CDTBM; hence, the electrostatic driving force for CT state splitting will be higher in IDTTBM. In addition, this force impedes geminate recombination of CT states and therefore should increase the short-circuit current, which is again observed experimentally.<sup>38</sup>

**Time-Resolved Spectroscopic Studies.** To understand the origin of the device performance difference across the two NFA systems, exciton and charge carrier dynamics were studied by time-resolved photoluminescence (TRPL) and transient absorption (TA) pump–probe spectroscopy. We specifically address the difference in photocurrent by transient spectroscopy across a time range from picoseconds to microseconds (ps– $\mu$ s). Using TA, exciton dissociation and fast (subnanosecond) charge recombination were examined on the picosecond–nanosecond (ps–ns) time scale, while slower recombination of spatially separated charges was investigated on the ns– $\mu$ s time scale.

**Exciton Quenching and Charge Transfer.** Steady-state PL (quenching) data is presented in Figure S6 for PCE10:IDTTBM and PCE10:CDTBM blends. We reported previously that the PL quenching in PCE10:CDTBM is around 99%.<sup>39</sup> Here, a further investigation of the exciton dynamics was performed by transient PL measurements on PCE10:IDTTBM blends following excitation at 600 nm using a Streak camera system. The transient PL spectra of the PCE10:IDTTBM blend are shown in Figure 3a for different time delays. The equivalent data of PCE10:CDTBM are shown in Figure S7. The blend spectra are broad and featureless and peak at 740 nm instantly after excitation. The spectra show a pronounced red shift in the first 16 ps, with another feature becoming apparent around 800 nm. The PL transients of neat IDTTBM and the blend were fitted with single exponentials; the associated PL lifetimes obtained from the fits are 97 and 36 ps, respectively, confirming the occurrence of exciton quenching in the blend. To obtain further insights into the spectral evolution, we plotted the normalized spectra of neat PCE10 and IDTTBM films alongside the spectra of the blend

as shown in Figure 3b. The features observed at 750 and 800 nm in the blend spectrum match the PL maxima of the donor and acceptor components. Hence, we conclude from the spectral shape that the observed PL spectra of the blend consist of convoluted spectra of both the donor polymer PCE10 and the acceptor IDTTBM, as both are present in the blend. In order to distinguish the contributions of the two components, we performed multivariate curve resolution (MCR) analysis.<sup>44</sup> The results of MCR are shown in Figure 3c. The component spectra obtained from MCR analysis are similar to the PL of the neat materials (see Figure 3b). However, we note that the peak position of component 1 as obtained from MCR analysis and assigned to the emission of PCE10 in the blend is blue-shifted compared to the experimentally determined steady-state PL spectrum of PCE10. We hypothesize this could be caused by dilution of PCE10 polymer chains in the blend with the NFA, leading to more disorder in the polymer and thus some emission from higher-lying sites in the density of states.

Furthermore, MCR was also used to determine the component-associated dynamics, which are depicted in Figure 3d for a time range of up to 100 ps, and in the inset up to 400 ps. Fitting the component-associated decays to single-exponential functions yields PL lifetimes of PCE10 and IDTTBM emission in the blend of 10 and 35 ps, respectively.

The fluorescence decays were further analyzed by a simple kinetic model (Figure S8), assuming that two parallel decay channels exist for the excitons, namely recombination to the ground state (via a combination of radiative and nonradiative processes) and charge transfer at the interface, creating charge-transfer states. We use this simple model here, because we found it accurately describes the PL dynamics. Furthermore, adding more decay processes would lead to overparametrization of the model, while not yielding additional insights. We denote the decay rate associated with the fluorescence of the excited state (exciton) to the ground state as  $k_F$ , and analogously the rate of charge transfer from the excited state to the interfacial CTstate as  $k_{CT}$ . Hence, the exciton quenching efficiency due to charge transfer can be deduced from the following expression:  $\varphi_{CT} = \frac{k_{CT}}{k_{CT} + k_F}$ . By fitting the PL decays of both components, we found for the concomitant excitation of PCE10 and IDTTBM ( $k_{CT} + k_F$ ) =  $1 \times 10^{11} \text{ s}^{-1}$  and  $2.9 \times 10^{10} \text{ s}^{-1}$ , respectively. The values of  $k_F$  were obtained from the PL transients of the neat materials as  $1.9 \times 10^{10} \text{ s}^{-1}$  for PCE10 and  $7.8 \times 10^9 \text{ s}^{-1}$  for IDTTBM, respectively. From these values  $k_{CT}$  was calculated, and the efficiencies  $\varphi(\text{CT}_{\text{PCE10}})$  and  $\varphi(\text{CT}_{\text{IDTTBM}})$  were estimated to be 82% and 73%, respectively. Thus, it appears that the charge-transfer efficiency from PCE10 to the acceptor, namely  $\varphi(\text{CT}_{\text{PCE10}})$ , is higher than from the acceptor to the donor polymer, namely  $\varphi(\text{CT}_{\text{IDTTBM}})$ . However, we note that because of the limited time-resolution of the Streak camera system (1–2 ps in our setup), mostly excitons, which did not immediately undergo ultrafast charge transfer, are monitored. In other words, excitons that undergo diffusion-limited dissociation are detected by our transient PL experiment. In comparison, for PCE10:CDTBM, values of  $\varphi(\text{CT}_{\text{PCE10}})$  and  $\varphi(\text{CT}_{\text{CDTBM}})$  were estimated as 66% and 50%, confirming that the charge-transfer efficiency is higher from PCE10 compared to that from the acceptor molecules CDTBM. Furthermore, the charge-transfer efficiency is higher, 82%, in the case of PCE10:IDTTBM compared to that estimated for PCE10:CDTBM, 66%, indicating more efficient exciton quenching from PCE10 in the former.

Picosecond–Nanosecond Exciton and Charge Carrier Dynamics.  
Figure 4a shows the ps–ns TA spectra for different delay times

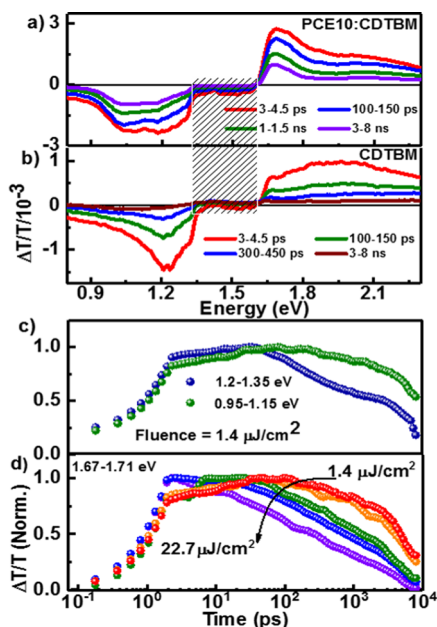


Figure 4. (a) Picosecond–nanosecond TA spectra of PCE10:CDTBM thin-film blends. (b) Picosecond–nanosecond TA spectra of pristine CDTBM film. (c) Charge carrier dynamics probed in spectral windows of 0.95–1.15 eV (green dots) and 1.2–1.35 eV (blue dots). Note that the band monitored at 1.2–1.35 eV exhibits clearly a faster decay. (d) Excited-state dynamics monitored at the position of the photo bleach band (1.67–1.71 eV) of the PCE10:CDTBM blend for different excitation fluences. Note: The shaded, highlighted area in panels a and b indicates the spectral region affected by the optical filters used to attenuate the probe spectrum in this region.

for a PCE10:CDTBM blend. The TA spectrum consists of the ground-state bleach (GSB) spanning the region from 1.6 to 2.2 eV and a broad photoinduced absorption (PA) in the spectral range of 0.95–1.35 eV peaking 3 ps after excitation. The decay of the PA was found to be faster in the spectral region of 1.2–1.35 eV compared to the spectral region of 0.95–1.15 eV, indicating that different states contribute to the PA. We assign the fast decay observed in the region between 1.2 and 1.35 eV to quenching and dissociation of CDTBM singlet excitons, while the slower decay is attributed to ps–ns charge recombination. This assignment is supported by TA experiments on thin films of the neat acceptor CDTBM as shown in Figure 4b and by the spectra of neat PCE10 shown in Figure S9. A broad and unstructured ground-state bleach band in the region of the CDTBM absorption is apparent in the neat film, which is different in shape from the GSB observed in the blend; however, it matches the TA observed from neat PCE10. Furthermore, the PA band observed for the neat CDTBM film is significantly narrower compared to the PA of neat PCE10 and the blend and it peaks around 1.22 eV. Here, we assign the PA in the region of 1.2–1.35 eV to exciton-induced absorption of CDTBM. When the spectra of the neat CDTBM film and the PCE10:CDTBM blend are compared, it becomes clear that the faster decaying PA feature in the blend is at the same spectral position as the exciton-induced absorption observed in the neat CDTBM film, hence the assignment of this part of the PA to excitons. We note that in the blend, the excitonic PA

feature vanishes after 300–450 ps, and thereafter the remaining PA signal is solely attributed to charge-induced absorption. Overall, 35% of the initial signal amplitude remains after 8 ns in the blend. We also note that a significant contribution to the blend's PA stems from PCE10 cations, which is supported by comparing the TA spectra to the absorption spectra of chemically oxidized PCE10 films as shown in Figure S10. In fact, the overall PA band is composed of PCE10 cation-induced absorption and CDTBM anion-induced absorption, as further confirmed from the anion-induced absorption of CDTBM of chemically reduced films of neat CDTBM.

In order to further investigate the charge carrier recombination, the associated kinetics is extracted at the respective bands as displayed in Figure 4c,d. More specifically, the fluence dependence of the dynamics is monitored for a series of fluences between 1.4 and 22.7  $\mu\text{J}/\text{cm}^2$ . Clearly, the charge carrier dynamics is fluence-dependent, indicating that non-geminate recombination dominates the dynamics on this time scale. A signal rise up to 50 ps at low fluences and 10 ps at high fluences is observed, indicating a contribution from diffusion-limited dissociation of excitons at the interface to the charge generation, as also indicated from TRPL experiments (vide supra). Figure 4c shows the charge carrier dynamics extracted from the spectral regions of 1.2–1.35 eV and 0.95–1.15 eV. Here, the higher-energy region exhibits a faster decay compared to the lower-energy region of the PA, as exemplified in Figure 4c for the lowest fluence of 1.4  $\mu\text{J}/\text{cm}^2$ .

Similarly, the TA spectra and dynamics were measured for PCE10:IDTTBM films as presented in Figure 5a. Here, the GSB spans a range of 1.6–2.2 eV and is effectively a superposition of the individual GSB bands of the donor polymer PCE10 and the acceptor IDTTBM (Figure S10), while the PA band is dominated by charge-induced absorption from PCE10 cations. Interestingly, the spectral region probed

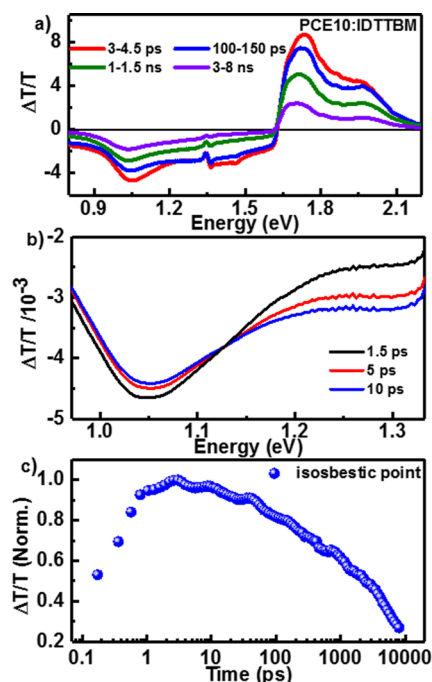
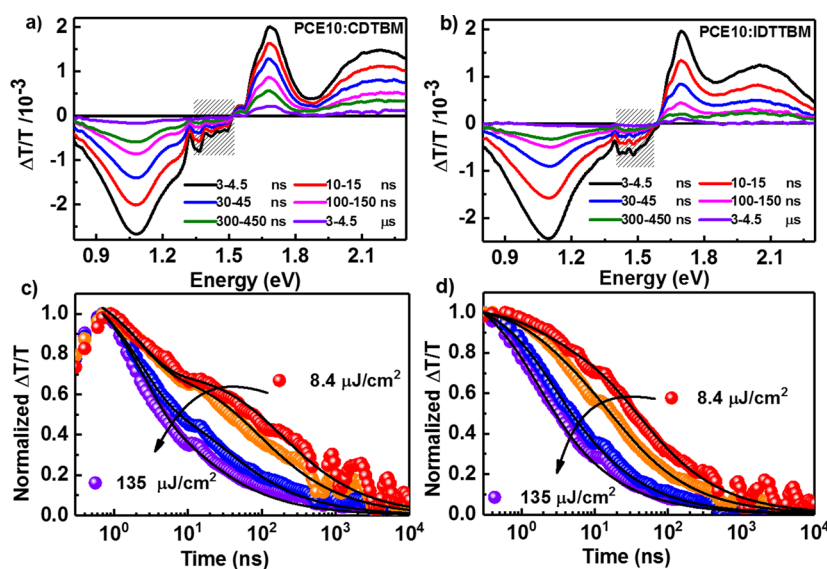


Figure 5. (a) Picosecond–nanosecond TA spectra of a PCE10:IDTTBM blend after excitation at 700 nm and (b) TA spectra of the PA region up to 10 ps, showing an isosbestic point at 1.14 eV. (c) TA dynamics monitored at 1.14 eV point.



**Figure 6.** Nanosecond–microsecond TA spectra for (a) PCE10:CDTBM and (b) PCE10:IDTTBM thin-film blends. Charge carrier dynamics monitored at 0.95–1.15 eV at different fluences (dots) and fits (solid lines) to a two-pool recombination model for (c) PCE10:CDTBM and (d) PCE10:IDTTBM blends. Note: The shaded highlighted area in panels a and b indicates the spectral region affected by the optical filters used to attenuate the probe spectrum in this region.

here shows no contribution from IDTTBM anions, as confirmed by separate absorption measurements on chemically reduced IDTTBM films (Figure S10). Here, the peak position of the PA band is at 1.05 eV, and a red-shift similar to that of the GSB is observed. We attribute this to the relaxation of charges to lower-energy sites. In addition to the bands mentioned above and in stark contrast to the experiments on CDTBM, an isosbestic point is observed at 1.14 eV in PCE10:IDTTBM, which is clearly seen in Figure 5b. The TA signal amplitude at the isosbestic point stays constant throughout the first 10 ps, while the TA signal (the PA) decays at higher probe photon energies and increases at lower probe photon energies. At the isosbestic point, the changes of the contributions of exciton-induced PA and charge-induced PA to the total signal amplitude cancel during charge transfer. In other words, the exciton-induced PA signal reduces, and simultaneously the charge-induced PA signal rises by the same amount; thus, the net change remains zero, and the total signal amplitude becomes an exclusive measure of the carrier recombination dynamics. The associated charge carrier dynamics monitored at the isosbestic point are depicted in Figure 5c; they correspond to the population of the charge carrier pool and indicate almost no charge carrier loss occurs in the first 10 ps. Furthermore, and in line with the results on CDTBM, the kinetics at low fluences show a rise up to 100 ps, a clear indication of diffusion-limited charge generation from excitons in pure PCE10 domains. On the other hand, for higher fluences such as 11.5  $\mu\text{J}/\text{cm}^2$ , the delayed (diffusion-limited) charge generation is less prominent and even absent for 23  $\mu\text{J}/\text{cm}^2$ , indicating the presence of exciton–charge annihilation and/or fast carrier recombination due to the high excited-state densities generated at higher fluences in the TA experiments. As shown in Figure 4c, the kinetics show an instantaneous rise and subsequent decay after 10 ps. We note that comparing the exciton lifetimes from TRPL experiments and charge generation dynamics from TA shows that the latter are faster compared to the former. As mentioned above, we hypothesize that the exciton quenching monitored by TRPL spectroscopy is

not representative for the entire pool of excitons, but only for the fraction which undergoes diffusion-limited dissociation. In other words, a large fraction of excitons, which is quenched ultrafast, faster than the time resolution of our Streak Camera system (about 2 ps), is not detected. That this fraction is not monitored by the TRPL experiment becomes obvious when looking at the PL quenching efficiency obtained from steady-state PL experiments on neat materials and blends, which demonstrate more than 98% exciton quenching in the PCE10:IDTTBM blend. Thus, the reduction in lifetime does not match the quenching observed in the TRPL experiment. However, TA is faster (a few hundred femtosecond time resolution) and thus monitors also the fraction of charges, which are quenched on a sub-1 ps time scale. For comparison, we have also presented the excited-state dynamics of the PCE10:IDTTBM in Figures S11 and S12.

**Nanosecond–Microsecond Charge Carrier Recombination.** The ns– $\mu\text{s}$  TA measurements were conducted to evaluate the charge carrier recombination in both photovoltaic systems on the time scale relevant for charge extraction from a photovoltaic device. The obtained spectra and dynamics are shown in Figure 6. Excitation of the blends was carried out at 532 nm with subnanosecond laser pulses. Notably, from the steady-state UV–vis absorption, both the donor and the acceptor exhibit absorption at this particular wavelength. The TA spectrum of PCE10:CDTBM exhibits a PA signal at 1.08 eV (Figure 6a). This PA band was assigned to charge-induced absorption in line with the assignment presented for the ps–ns TA experiments, because on this time scale charges represent the main population in the blend. Furthermore, a ground-state bleach was observed in the same spectral region as reported for the ps–ns TA experiments. Interestingly, we observe that in the case of CDTBM the early time dynamics up to 1.5 ns exhibit only slight intensity dependence in contrast to the ps–ns dynamics. This indicates that geminate recombination dominates at early times after photoexcitation on the ns– $\mu\text{s}$  time range, which is not observed in the case of the PCE10:IDTTBM blend system (Figure 6b). However, we

note that in the ns– $\mu$ s time window the resolution of our setup is limited to about 1 ns because of the laser pulse length, and excitation was performed at 532 nm because of experimental limitations. Furthermore, the shorter excitation laser pulse length (about 100 fs) used in the ps–ns TA experiments typically causes exciton–exciton and exciton–charge annihilation with increasing fluence.

The fluence dependence of the charge-induced absorption dynamics is further analyzed by fitting the data to a two-pool recombination model as previously introduced by Howard et al.<sup>45</sup> The fits to the experimental data from PCE10:CDTBM and PCE10:IDTTBM blends are depicted as solid lines in panels c and d of Figure 6, respectively.<sup>45</sup> The two-pool recombination model used here accounts for both geminate and nongeminate recombination processes, considered as two independent populations; however, they are spectrally indistinguishable. As demonstrated previously, under these boundary conditions, the charge carrier dynamics can be described by the following equation:

$$Y = (N_0(1 - f)[1 - \exp(-k_{CT \rightarrow GS})] + N_0 f - [\lambda \gamma t + (f N_0)^{-\lambda}]^{1/\lambda}) / N_0 \quad (1)$$

Herein,  $k_{CT \rightarrow GS}$  is the monomolecular (geminate) rate constant,  $\lambda$  is the nongeminate recombination order,  $\gamma$  is the nongeminate coefficient,  $f$  is the fraction of charges that undergo nongeminate recombination, and  $N_0$  is the total initial population of charges. The values of  $N_0$  can be approximated from the fluences and the absorbance of the thin-film sample at the excitation wavelength as shown in the Supporting Information, Table S2; however, they may be overestimated as recombination can also occur within the subnanosecond excitation pulse. Thus, the values of  $N_0$  were allowed to vary within small boundaries during data fitting to account for this effect. When the experimentally measured charge-induced absorption dynamics are fit to eq 1, the recombination parameters are determined. A summary of all the extracted fitting parameters is provided in Table 2.

**Table 2. Recombination Parameters Extracted from the Two-Pool Model Fit to the Experimental Data of PCE10:CDTBM and PCE10:IDTTBM Thin-Film Blends**

parameter	PCE10:CDTBM	PCE10:IDTTBM
$f$	$0.76 \pm 0.01$	$0.89 \pm 0.01$
$1 - f$	0.24	0.11
$k$ ( $s^{-1}$ )	$7.7 \times 10^7 \pm 1.34 \times 10^7$	$5.8 \times 10^8 \pm 1 \times 10^6$
$\lambda + 1$	$2.51 \pm 0.01$	$2.59 \pm 0.01$
$\gamma$ ( $cm^3$ ) <sup><math>\lambda</math></sup> $s^{-1}$	$1.8 \times 10^{-21} \pm 4.42 \times 10^{-21}$	$1 \times 10^{-21} \pm 1.87 \times 10^{-23}$
$\beta$ ( $cm^3 s^{-1}$ )	$1.83 \times 10^{-13}$	$1.63 \times 10^{-12}$

The fitting parameters indicate that the CTstate lifetimes are different for the two blend systems studied here. PCE10:CDTBM exhibit an inverse rate constant of 13 ns, while 2 ns is determined for PCE10:IDTTBM. The latter can be considered instrument-limited, as for the ns– $\mu$ s TA experiments an excitation pulse of about 1 ns was used. The longer CTstate lifetime observed for PCE10:CDTBM can be rationalized by a larger electron–hole separation, similar to what has been observed by Howard et al. in annealed RR-P3HT:PCBM blends.<sup>45</sup> In addition, some charges may be generated in regions of the bulk heterojunction that are not connected to the charge percolation network. These charges

undergo quasi-geminate recombination on a longer time scale. Furthermore, the direct comparison of the two blend systems indicates that 24% of the charges in PCE10:CDTBM undergo geminate recombination, while in PCE10:IDTTBM it is only 11%. The reason for the larger fraction of geminate recombination in the PCE10:CDTBM blend can be understood when considering the results of the DFT calculations. They demonstrate that the quadrupole moment of IDTTBM is almost twice as large as that of CDTBM; hence, the electrostatic driving force for CTstate splitting is almost two times higher in IDTTBM. This force impedes geminate recombination of CT states and therefore increases the short-circuit current. Importantly, the substantial difference in the amount of geminate recombination is in good agreement with the experimentally observed difference in the short-circuit currents of the two blend systems. In fact, the extracted fractions of nongeminate recombination of 76% and 89% for PCE10:CDTBM and PCE10:IDTTBM as acceptor are similar to the experimentally determined IQE values of the two systems, estimated to be 74% and 90%, respectively. Clearly, this indicates that the free charges that undergo nongeminate recombination in the TA experiment could potentially be extracted as photocurrent from a device. Here, we argue that, as the fill factor of devices is high, nongeminate recombination does not appear to compete significantly with carrier extraction. Hence, the IQE matches the fraction of free charges obtained from TA experiments, as they can be extracted and as charge generation itself does not appear to be field-dependent between  $V_{oc}$  and  $J_{sc}$  conditions. Additionally, the effective bimolecular recombination coefficients (at a carrier concentration roughly equivalent to 1 sun) were calculated to be  $1.83 \times 10^{-13}$  and  $1.63 \times 10^{-12} \text{ cm}^3 \text{ s}^{-1}$  for PCE10:CDTBM and PCE10:IDTTBM, respectively. A difference of a factor of 9 indicates that nongeminate recombination is faster (at the same carrier density) in PCE10:IDTTBM, which we ascribe to some extent to the higher charge carrier mobility in this system. We note that in the Langevin recombination model, increasing the mobility of charges increases the bimolecular recombination rate, in line with our results. However, at the same time the charge extraction is also faster; hence, charge extraction can outcompete nongeminate recombination. MIS-CELIV (metal insulator semiconductor-charge extraction by linearly increasing voltage) was employed to determine the carrier mobility, and for both acceptors, the electron mobility was determined to be  $3 \times 10^{-5} \text{ cm}^2 \text{ V}^{-1} \text{ s}^{-1}$ , while the hole mobility of PCE10:IDTTBM was found to be  $\sim 1.6 \times 10^{-3} \text{ cm}^2 \text{ V}^{-1} \text{ s}^{-1}$ , that is, approximately a factor of 3 higher with respect to the PCE10:CDTBM-based devices ( $4.2 \times 10^{-4} \text{ cm}^2 \text{ V}^{-1} \text{ s}^{-1}$ ). In summary, the higher nongeminate recombination rate does not appear to lead to substantial carrier recombination losses in an operating device at 1 sun illumination conditions, likely because the carrier mobility is sufficient to extract carriers prior to nongeminate recombination.

In conclusion, we have elucidated the origin of the performance increase in PCE10:NFA systems upon changing the acceptor core structure from CDT to IDTT. The higher open-circuit voltage of the IDTT acceptor-based BHJ solar cell is explained by a higher interfacial CTstate energy, while an increased short-circuit current was found to be a consequence of reduced geminate recombination as revealed by transient absorption spectroscopy. The fill factors of the two blend systems are similar, and both are in excess of 60%, indicating that field-dependent charge generation and nongeminate

recombination competing with charge extraction are of minor importance in terms of influence on device performance. Our results demonstrate that the core of the NFA acceptor can have significant impact on the efficiency-limiting processes in polymer:NFA systems and thus on device performance, despite similar light-harvesting properties. In particular, the IDTT-based acceptor has a longer core and hence a larger quadrupole moment, which facilitates interfacial CTstate splitting and charge generation and reduces geminate recombination. In contrast to CDT, IDTTBM does not have a ground-state dipole moment. This reduces the width of the density of states of this acceptor and leads to a smaller reduction of  $V_{oc}$  with respect to the photovoltaic gap of the blend. Our results point to the idea that the core of the NFA mediates not only the polymer–NFA interactions at the interface but also the interfacial energetic landscape and thereby the efficiency of splitting of CT states, charge separation, and recombination at the interface.

## ■ ASSOCIATED CONTENT

### 📄 Supporting Information

The Supporting Information is available free of charge on the ACS Publications website at DOI: 10.1021/acseenergylett.8b00045.

Experimental section, PCE10:PCBM internal quantum efficiency spectra, ellipsometry, steady-state PL, DFT calculations, TRPL spectra of PCE10:CDTBM, calculation of internal quantum efficiency, kinetic model of decay channels, transmission spectra of oxidized/reduced materials, TA spectra of neat PCE10, and determination of initial carrier densities  $N_0$  for two-pool model fits (PDF)

## ■ AUTHOR INFORMATION

### Corresponding Author

\*E-mail: frederic.laquai@kaust.edu.sa. Webpage, Ultrafast Dynamics Group: <https://ufd.kaust.edu.sa>.

### ORCID

Jafar I. Khan: 0000-0001-6003-5641

Denis Andrienko: 0000-0002-1541-1377

Pierre M. Beaujuge: 0000-0003-2868-4494

Frédéric Laquai: 0000-0002-5887-6158

### Notes

The authors declare no competing financial interest.

## ■ ACKNOWLEDGMENTS

The research reported in this publication was supported by the Office of Sponsored Research (OSR) under the Grant Agreement FCS/1/3321/01 and by the King Abdullah University of Science and Technology (KAUST). M.A.A. is grateful to Saudi Basic Industries Corporation (SABIC) for funding received towards the Ph.D.

## ■ REFERENCES

- (1) Yu, G.; Gao, J.; Hummelen, J. C.; Wudl, F.; Heeger, A. J. Polymer Photovoltaic Cells: Enhanced Efficiencies via a Network of Internal Donor-Acceptor Heterojunctions. *Science* **1995**, *270*, 1789–1791.
- (2) He, M.; Han, W.; Ge, J.; Yang, Y.; Qiu, F.; Lin, Z. All-Conjugated Poly(3-Alkylthiophene) Diblock Copolymer-Based Bulk Heterojunction Solar Cells with Controlled Molecular Organization and Nanoscale Morphology. *Energy Environ. Sci.* **2011**, *4*, 2894–2902.
- (3) He, M.; Han, W.; Ge, J.; Yu, W.; Yang, Y.; Qiu, F.; Lin, Z. Annealing Effects on The Photovoltaic Performance of All-Conjugated Poly(3-Alkylthiophene) Diblock Copolymer-Based Bulk Heterojunction Solar Cells. *Nanoscale* **2011**, *3*, 3159–3163.
- (4) Vohra, V.; Kawashima, K.; Kakara, T.; Koganezawa, T.; Osaka, I.; Takimiya, K.; Murata, H. Efficient Inverted Polymer Solar Cells Employing Favourable Molecular Orientation. *Nat. Photonics* **2015**, *9*, 403–408.
- (5) You, J.; Dou, L.; Yoshimura, K.; Kato, T.; Ohya, K.; Moriarty, T.; Emery, K.; Chen, C.-C.; Gao, J.; Li, G.; et al. A Polymer Tandem Solar Cell with 10.6% Power Conversion Efficiency. *Nat. Commun.* **2013**, *4*, 1446.
- (6) He, Z.; Xiao, B.; Liu, F.; Wu, H.; Yang, Y.; Xiao, S.; Wang, C.; Russell, T. P.; Cao, Y. Single-Junction Polymer Solar Cells with High Efficiency and Photovoltage. *Nat. Photonics* **2015**, *9*, 174–179.
- (7) Zhao, J.; Li, Y.; Yang, G.; Jiang, K.; Lin, H.; Ade, H.; Ma, W.; Yan, H. Efficient Organic Solar Cells Processed from Hydrocarbon Solvents. *Nat. Energy* **2016**, *1*, 15027.
- (8) Facchetti, A. Polymer Donor–Polymer Acceptor (All-Polymer) Solar Cells. *Mater. Today* **2013**, *16*, 123–132.
- (9) Zhou, H.; Zhang, Y.; Mai, C.-K.; Collins, S. D.; Bazan, G. C.; Nguyen, T.-Q.; Heeger, A. J. Polymer Homo-Tandem Solar Cells with Best Efficiency of 11.3%. *Adv. Mater.* **2015**, *27*, 1767–1773.
- (10) Verreert, B.; Cnops, K.; Cheyens, D.; Heremans, P.; Stesmans, A.; Zango, G.; Claessens, C. G.; Torres, T.; Rand, B. P. Decreased Recombination Through the Use of a Non-Fullerene Acceptor in a 6.4% Efficient Organic Planar Heterojunction Solar Cell. *Adv. Energy Mater.* **2014**, *4*, 1301413.
- (11) Bloking, J. T.; Giovenzana, T.; Higgs, A. T.; Ponc, A. J.; Hoke, E. T.; Vandewal, K.; Ko, S.; Bao, Z.; Sellinger, A.; McGehee, M. D. Comparing the Device Physics and Morphology of Polymer Solar Cells Employing Fullerenes and Non-Fullerene Acceptors. *Adv. Energy Mater.* **2014**, *4*, 1301426.
- (12) Bin, H.; Gao, L.; Zhang, Z.-G.; Yang, Y.; Zhang, Y.; Zhang, C.; Chen, S.; Xue, L.; Yang, C.; Xiao, M.; et al. 11.4% Efficiency Non-Fullerene Polymer Solar Cells with Trialkylsilyl Substituted 2D-Conjugated Polymer as Donor. *Nat. Commun.* **2016**, *7*, 13651.
- (13) Holliday, S.; Ashraf, R. S.; Wadsworth, A.; Baran, D.; Yousaf, S. A.; Nielsen, C. B.; Tan, C.-H.; Dimitrov, S. D.; Shang, Z.; Gasparini, N.; et al. High-Efficiency and Air-Stable P3HT-Based Polymer Solar Cells with a New Non-Fullerene Acceptor. *Nat. Commun.* **2016**, *7*, 11585.
- (14) Nielsen, C. B.; Holliday, S.; Chen, H.-Y.; Cryer, S. J.; McCulloch, I. Non-Fullerene Electron Acceptors for Use in Organic Solar Cells. *Acc. Chem. Res.* **2015**, *48*, 2803–2812.
- (15) Bin, H.; Zhang, Z.-G.; Gao, L.; Chen, S.; Zhong, L.; Xue, L.; Yang, C.; Li, Y. Non-Fullerene Polymer Solar Cells Based on Alkylthio and Fluorine Substituted 2D-Conjugated Polymers Reach 9.5% Efficiency. *J. Am. Chem. Soc.* **2016**, *138*, 4657–4664.
- (16) Hu, H.; Jiang, K.; Chow, P. C. Y.; Ye, L.; Zhang, G.; Li, Z.; Carpenter, J. H.; Ade, H.; Yan, H. Influence of Donor Polymer on the Molecular Ordering of Small Molecular Acceptors in Nonfullerene Polymer Solar Cells. *Adv. Energy Mater.* **2018**, *8*, 1701674.
- (17) Li, Z.; Jiang, K.; Yang, G.; Lai, J. Y. L.; Ma, T.; Zhao, J.; Ma, W.; Yan, H. Donor Polymer Design Enables Efficient Non-Fullerene Organic Solar Cells. *Nat. Commun.* **2016**, *7*, 13094.
- (18) Zhao, W.; Qian, D.; Zhang, S.; Li, S.; Inganäs, O.; Gao, F.; Hou, J. Fullerene-Free Polymer Solar Cells with over 11% Efficiency and Excellent Thermal Stability. *Adv. Mater.* **2016**, *28*, 4734–4739.
- (19) Chen, S.; Liu, Y.; Zhang, L.; Chow, P. C. Y.; Wang, Z.; Zhang, G.; Ma, W.; Yan, H. A Wide-Bandgap Donor Polymer for Highly Efficient Non-Fullerene Organic Solar Cells with a Small Voltage Loss. *J. Am. Chem. Soc.* **2017**, *139*, 6298–6301.
- (20) Zhao, W.; Li, S.; Yao, H.; Zhang, S.; Zhang, Y.; Yang, B.; Hou, J. Molecular Optimization Enables over 13% Efficiency in Organic Solar Cells. *J. Am. Chem. Soc.* **2017**, *139*, 7148–7151.
- (21) Sauvé, G.; Fernando, R. Beyond Fullerenes: Designing Alternative Molecular Electron Acceptors for Solution-Processable

Bulk Heterojunction Organic Photovoltaics. *J. Phys. Chem. Lett.* **2015**, *6*, 3770–3780.

(22) Zhang, X.; Lu, Z.; Ye, L.; Zhan, C.; Hou, J.; Zhang, S.; Jiang, B.; Zhao, Y.; Huang, J.; Zhang, S.; et al. A Potential Perylene Diimide Dimer-Based Acceptor Material for Highly Efficient Solution-Processed Non-Fullerene Organic Solar Cells with 4.03% Efficiency. *Adv. Mater.* **2013**, *25*, 5791–5797.

(23) Li, S.; Zhang, Z.; Shi, M.; Li, C.-Z.; Chen, H. Molecular Electron Acceptors for Efficient Fullerene-Free Organic Solar Cells. *Phys. Chem. Chem. Phys.* **2017**, *19*, 3440–3458.

(24) Li, S.; Ye, L.; Zhao, W.; Zhang, S.; Mukherjee, S.; Ade, H.; Hou, J. Energy-Level Modulation of Small-Molecule Electron Acceptors to Achieve over 12% Efficiency in Polymer Solar Cells. *Adv. Mater.* **2016**, *28*, 9423–9429.

(25) Lin, Y.; Zhao, F.; He, Q.; Huo, L.; Wu, Y.; Parker, T. C.; Ma, W.; Sun, Y.; Wang, C.; Zhu, D.; et al. High-Performance Electron Acceptor with Thienyl Side Chains for Organic Photovoltaics. *J. Am. Chem. Soc.* **2016**, *138*, 4955–4961.

(26) Chen, W.; Zhang, Q. Recent Progress in Non-Fullerene Small Molecule Acceptors in Organic Solar Cells (Oscs). *J. Mater. Chem. C* **2017**, *5*, 1275–1302.

(27) Liu, T.; Meng, D.; Cai, Y.; Sun, X.; Li, Y.; Huo, L.; Liu, F.; Wang, Z.; Russell, T. P.; Sun, Y. High-Performance Non-Fullerene Organic Solar Cells Based on a Selenium-Containing Polymer Donor and a Twisted Perylene Bisimide Acceptor. *Adv. Science* **2016**, *3*, 1600117.

(28) Yao, H.; Chen, Y.; Qin, Y.; Yu, R.; Cui, Y.; Yang, B.; Li, S.; Zhang, K.; Hou, J. Design and Synthesis of a Low Bandgap Small Molecule Acceptor for Efficient Polymer Solar Cells. *Adv. Mater.* **2016**, *28*, 8283–8287.

(29) Bauer, N.; Zhang, Q.; Zhao, J.; Ye, L.; Kim, J.-H.; Constantinou, I.; Yan, L.; So, F.; Ade, H.; Yan, H.; You, W. Comparing Non-Fullerene Acceptors with Fullerene in Polymer Solar Cells: A Case Study with FTAZ and Pycntaz. *J. Mater. Chem. A* **2017**, *5*, 4886–4893.

(30) Zhang, S.; Ye, L.; Zhao, W.; Liu, D.; Yao, H.; Hou, J. Side Chain Selection for Designing Highly Efficient Photovoltaic Polymers with 2D-Conjugated Structure. *Macromolecules* **2014**, *47*, 4653–4659.

(31) Clarke, T. M.; Durrant, J. R. Charge Photogeneration in Organic Solar Cells. *Chem. Rev.* **2010**, *110*, 6736–6767.

(32) Deibel, C.; Strobel, T.; Dyakonov, V. Role of the Charge Transfer State in Organic Donor–Acceptor Solar Cells. *Adv. Mater.* **2010**, *22*, 4097–4111.

(33) Burke, T. M.; Sweetnam, S.; Vandewal, K.; McGehee, M. D. Beyond Langevin Recombination: How Equilibrium Between Free Carriers and Charge Transfer States Determines the Open-Circuit Voltage of Organic Solar Cells. *Adv. Energy Mater.* **2015**, *5*, 1500123.

(34) Gehrig, D. W.; Howard, I. A.; Laquai, F. Charge Carrier Generation Followed by Triplet State Formation, Annihilation, and Carrier Recombination in PBDTTT-C/PC60BM Photovoltaic Blends. *J. Phys. Chem. C* **2015**, *119*, 13509–13515.

(35) Poelking, C.; Andrienko, D. Long-Range Embedding of Molecular Ions and Excitations in a Polarizable Molecular Environment. *J. Chem. Theory Comput.* **2016**, *12*, 4516–4523.

(36) D'Avino, G.; Muccioli, L.; Castet, F.; Poelking, C.; Andrienko, D.; Soos, Z. G.; Cornil, J.; Beljonne, D. Electrostatic Phenomena in Organic Semiconductors: Fundamentals and Implications for Photovoltaics. *J. Phys. Condens. Matter* **2016**, *28*, 433002.

(37) Poelking, C.; Tietze, M.; Elschner, C.; Olthof, S.; Hertel, D.; Baumeier, B.; Würthner, F.; Meerholz, K.; Leo, K.; Andrienko, D. Impact of Mesoscale Order on Open-Circuit Voltage in Organic Solar Cells. *Nat. Mater.* **2015**, *14*, 434.

(38) Poelking, C.; Andrienko, D. Design Rules for Organic Donor–Acceptor Heterojunctions: Pathway for Charge Splitting and Detrapping. *J. Am. Chem. Soc.* **2015**, *137*, 6320–6326.

(39) Wang, K.; Firdaus, Y.; Babics, M.; Cruciani, F.; Saleem, Q.; El Labban, A.; Alamoudi, M. A.; Marszalek, T.; Pisula, W.; Laquai, F.; et al.  $\pi$ -Bridge-Independent 2-(Benzo[c][1,2,5]thiadiazol-4-ylmethylene)malononitrile-Substituted Nonfullerene Acceptors for

Efficient Bulk Heterojunction Solar Cells. *Chem. Mater.* **2016**, *28*, 2200–2208.

(40) Bai, H.; Wu, Y.; Wang, Y.; Wu, Y.; Li, R.; Cheng, P.; Zhang, M.; Wang, J.; Ma, W.; Zhan, X. Nonfullerene Acceptors Based on Extended Fused Rings Flanked with Benzothiadiazolylmethylene-malononitrile for Polymer Solar Cells. *J. Mater. Chem. A* **2015**, *3*, 20758–20766.

(41) Jagadamma, L. K.; Abdelsamie, M.; El Labban, A.; Aresu, E.; Ngongang Ndjawa, G. O.; Anjum, D. H.; Cha, D.; Beaujuge, P. M.; Amassian, A. Efficient Inverted Bulk-Heterojunction Solar Cells from Low-Temperature Processing of Amorphous ZnO Buffer Layers. *J. Mater. Chem. A* **2014**, *2*, 13321–13331.

(42) Vandewal, K.; Tvingstedt, K.; Gadisa, A.; Inganäs, O.; Manca, J. V. On The Origin of The Open-Circuit Voltage of Polymer-Fullerene Solar Cells. *Nat. Mater.* **2009**, *8*, 904–909.

(43) Vandewal, K.; Tvingstedt, K.; Gadisa, A.; Inganäs, O.; Manca, J. V. Relating The Open-Circuit Voltage to Interface Molecular Properties of Donor:Acceptor Bulk Heterojunction Solar Cells. *Phys. Rev. B: Condens. Matter Mater. Phys.* **2010**, *81*, 125204.

(44) Jaumot, J.; Gargallo, R.; de Juan, A.; Tauler, R. A Graphical User-Friendly Interface For MCR-ALS: A New Tool for Multivariate Curve Resolution in MATLAB. *Chemom. Intell. Lab. Syst.* **2005**, *76*, 101–110.

(45) Howard, I. A.; Mauer, R.; Meister, M.; Laquai, F. Effect of Morphology on Ultrafast Free Carrier Generation in Polythiophene-Fullerene Organic Solar Cells. *J. Am. Chem. Soc.* **2010**, *132*, 14866–14876.